Published in final edited form as:
Magn Reson Med. 2013 November ; 70(5): . doi:10.1002/mrm.24592.

High-Frequency Subband Compressed Sensing MRI Using Quadruplet Sampling

Kyunghyun Sung[1,2,*] and **Brian A Hargreaves**[1]

[1]Department of Radiology, Stanford University, Stanford, California, USA

[2]Department of Radiological Sciences, University of California Los Angeles, Los Angeles, California, USA

Abstract

Purpose—To presents and validates a new method that formalizes a direct link between k-space and wavelet domains to apply separate undersampling and reconstruction for high- and low-spatial-frequency k-space data.

Theory and Methods—High- and low-spatial-frequency regions are defined in k-space based on the separation of wavelet subbands, and the conventional compressed sensing (CS) problem is transformed into one of localized k-space estimation. To better exploit wavelet-domain sparsity, CS can be used for high-spatial-frequency regions while parallel imaging can be used for low-spatial-frequency regions. Fourier undersampling is also customized to better accommodate each reconstruction method: random undersampling for CS and regular undersampling for parallel imaging.

Results—Examples using the proposed method demonstrate successful reconstruction of both low-spatial-frequency content and fine structures in high-resolution 3D breast imaging with a net acceleration of 11 to 12.

Conclusion—The proposed method improves the reconstruction accuracy of high-spatial-frequency signal content and avoids incoherent artifacts in low-spatial-frequency regions. This new formulation also reduces the reconstruction time due to the smaller problem size.

Keywords

Image reconstruction; Compressed sensing; Wavelet transformation; Parallel imaging; Iterative reconstruction

Introduction

The speed of magnetic resonance imaging (MRI) is critical in many clinical applications and depends on the amount of acquired k-space data. However, if one does not fully acquire k-space data, the MR image using a conventional Fourier reconstruction experiences aliasing artifacts whose severity depends on the k-space undersampling pattern used. However, these artifacts can be reduced by using sampling and reconstruction techniques that exploit information redundancy or prior knowledge.

One common way to mitigate the undersampling artifacts is to design sampling trajectories that produce less visually prominent aliasing artifacts, often called incoherent artifacts.

[*]Correspondence to: UCLA Department of Radiological Sciences 300 UCLA Medical Plaza, Suite B119 Los Angeles, CA 90095 Phone: (310) 267-6842 Fax: (310) 825-9118 ksung@mednet.ucla.edu.

Typically by using irregular k-space sampling such as projection reconstruction imaging (1, 2), variable density spiral imaging (3), or random sampling (4), aliasing can be made less coherent than in Cartesian imaging. A point spread function is commonly used to evaluate the undersampling trajectories, where dominant side lobe amplitudes are associated with more coherent aliasing. However, selection of the irregular sampling pattern can be heuristic, and application-dependent. The severity of artifacts is often subjective, and their noise-like behavior can make it difficult to distinguish them from real signal.

Many reconstruction methods have been proposed to further reduce the undersampling artifacts by exploiting prior knowledge. Partial k-space reconstruction synthesizes uncollected k-space data by using Hermitian symmetry after applying a phase correction (5, 6). Parallel imaging has been widely used to reconstruct undersampled k-space data, acquired from multiple coils with spatially-varying sensitivities, using knowledge of the coil sensitivities or data correlation between coils (7–9).

Compressed sensing (CS) is an alternative acquisition and reconstruction technique to Nyquist sampling that can dramatically reduce the measurement size without causing aliasing artifacts when the underlying signal is sparse (10, 11). Its promise to improve the speed of MRI has been successfully demonstrated using a wavelet transform (12). However, depending on implementation and application, conventional CS MRI is limited in some cases by complexity of integration with parallel imaging (13–24), residual incoherent artifacts due to possible reconstruction failure (25), and high computational costs for the reconstruction (26).

In this paper, we describe a novel undersampling and reconstruction scheme to address the above issues. Our proposed k-space undersampling scheme (quadruplet sampling) enables k-space data to be decomposed into local regions that correspond to different wavelet subbands using the time-frequency localization of wavelet transforms. Our new reconstruction method (high-frequency subband CS) then transforms the original L1-minimization problem to reduce both its size and complexity, and independently estimates each localized region of k-space data.

We combine CS and parallel imaging by employing different methods in different k-space regions: parallel imaging for low-spatial-frequencies and CS for high-spatial-frequencies. This localized method is an efficient way to combine both methods since it allows selective application of different undersampling patterns and reconstructions in different k-space regions. This not only improves the reconstruction accuracy by exploiting the wavelet sparsity characteristics (27) and the wavelet tree structure (28–30), but also avoids possible CS failure in the low-spatial-frequency region by applying parallel imaging in the low-spatial-frequency region. In addition, the computational complexity is lower, mainly due to the smaller problem size. Applied to high-resolution 3D breast imaging, we demonstrate that this method successfully recovers image features with a net acceleration factor of 11 to 12.

THEORY

Compressed Sensing MRI

CS allows accurate reconstruction of images with far fewer measurements than traditional methods when two requirements are met: sparsity and incoherence (10, 11, 27). Sparsity refers to the fact that the image information can be represented using a small number of coefficients without compromising the image quality. Incoherence expresses the idea that the energy of objects in the sparse representation domain is spread out in the measurement domain. Practical CS MRI typically employs a wavelet transform to promote sparsity, and random k-space sampling to ensure incoherence (12). If conditions of sparsity and

incoherence are satisified, an image can be recovered to high accuracy, even when k-space is significantly undersampled, by solving the following convex optimization:

$$\min_x \|\Psi x\|_1, \quad \text{subject to} \|y - \Phi x\|_2 < \epsilon. \quad (1)$$

Here, y consists of the acquired k-space samples, x is a 2D or 3D image, Φ is the undersampled Fourier transform, Ψ is a sparse transformation such as a wavelet transform or a total variation, and ϵ bounds the amount of noise in the measurement.

Denoting Ψ and Ψ^{-1} for the forward and inverse wavelet transform, wavelet coefficients w are related to an image x by $w = \Psi x$ or $x = \Psi^{-1} w$, and Eq. 1 can be rewritten in terms of w instead of x:

$$\min_w \|w\|_1, \quad \text{subject to} \|y - \Phi\Psi^{-1} w\| < \epsilon. \quad (2)$$

Note that the minimization in Eq. 2 includes two domains, wavelet (sparse basis) and k-space (data acquisition), where the two domains are connected by the inverse wavelet transform followed by the undersampled Fourier transform ($\Phi\Psi^{-1}$), which we refer to as a Fourier-Wavelet transform. We first describe mathematical derivations on the Fourier-Wavelet transform using a one-dimensional signal to explain the wavelet subband decomposition, a key operation of this work. More details on wavelet basis functions of the continuous and discrete wavelet transforms are described in Appendix **A**.

1D Fourier-Wavelet Transform, $\Phi\Psi^{-1}$—The fast wavelet transform can be implemented using discrete filters, $h[n]$ and $g[n]$, a pair of quadrature mirror filters (low and high pass filters), if the form of scaling and wavelet function is known. If we use the notation $[\cdot]_{\downarrow 2}$ as downsampling by a factor of 2 (only even samples are kept), $[\cdot]_{\uparrow 2}$ as upsampling by a factor of 2 (insert one zero between each two samples) and $\star$ as discrete convolution, the approximation coefficients c_j and the detailed coefficients w_j at an arbitrary scale j can be computed by,

$$\begin{aligned} c_j &= \left[c_{j+1} \star \overline{h}\right]_{\downarrow 2} \\ w_j &= [c_{j+1} \star \overline{g}]_{\downarrow 2}, \end{aligned} \quad (3)$$

where $\overline{h}$ and $\overline{g}$ are defined as $h[-n]$ and $g[-n]$. We can also generalize the fast inverse transform by introducing biorthogonal bases,

$$c_{j+1} = [w_j]_{\downarrow 2} \star \overline{g}_1 + [c_j]_{\uparrow 2} \star \overline{h}_1. \quad (4)$$

where $\overline{h}_1$ and $\overline{g}_1$ are defined to be dual to $\overline{h}$ and $\overline{g}$. Note that the biorthogonal wavelet transform becomes orthogonal when $h = h_1$ and $g = g_1$. Figure 1a shows a schematic diagram to realize the fast wavelet transform (an orthogonal basis) with a single scale using a one-dimensional discrete signal $x[n]$, defined in [0, N-1].

When the Fourier transform (FT) is applied, we can explore the subband coding (analysis) and decoding (synthesis) in frequency domain (Figure 1b). After multiplying spectral weightings $\left(D_H = FT\{\overline{g}\}\right.$ and $\left.D_L = FT\left\{\overline{h}\right\}\right)$ to the one-dimensional k-space data y, defined in [–N/2, N/2-1], and downsampling by 2, we can describe y_3 and y_7 as,

$$\begin{aligned} y_3[k] &= (y_2[k/2] + y_2[k/2 - N/4])/2 \\ y_7[k] &= (y_6[k/2] + y_6[k/2 - N/4])/2, \end{aligned} \quad (5)$$

where $y_3 = FT\{w_0\}$ and $y_7 = FT\{c_0\}$, defined in [–N/4, N/4-1]. With upsampling and multiplying by the spectral weightings, we can express y as a sum of two components,

$$y = D_H \cdot y_4 + D_L \cdot y_8, \quad (6)$$

where y_4 and y_8 are the decomposed k-space data, corresponding to h and g.

We can decompose y into y_4 and y_8 as long as we sample both k_1 and k_2, where k_1 is any integer between –N/4 and N/4-1, and k_2 is a periodic location of k_1 with fundamental period N/2 (i.e., $k_2 = k_1 - N/2$ if $k_1 \geq 0$ and $k_2 = k_1 + N/2$ if $k_1 < 0$). Introducing notation $u_{H2} = y_4$ and $u_{L2} = y_8$ (equivalently, $u_H = y_3$ and $u_L = y_7$), the upsampling assures u_n and u_{n2} have the same value at the two locations,

$$\begin{aligned} u_L[k_1] &= u_{L2}[k_1] = u_{L2}[k_2] \\ u_H[k_1] &= u_{H2}[k_1] = u_{H2}[k_2], \end{aligned} \quad (7)$$

and y can be formulated in a matrix-vector form using Eq. 6:

$$\begin{pmatrix} y[k_1] \\ y[k_2] \end{pmatrix} = \begin{pmatrix} D_L[k_1] & D_H[k_1] \\ D_L[k_2] & D_H[k_2] \end{pmatrix} \begin{pmatrix} u_L[k_1] \\ u_H[k_1] \end{pmatrix}. \quad (8)$$

All the spectral weightings (D_L and D_H) are known based on the wavelet basis, and u_L and u_H can be computed by inverting the matrix **D**, called the wavelet subband decomposition. This wavelet decomposition is always possible when we sample both k_1 and k_2, and, by definition, u_L and u_H have a direct Fourier relationship with wavelet subbands, c_0 and w_0. Note that **D** is typically close to a diagonal matrix and becomes exactly diagonal if the wavelet filters have zero-transition-band (i.e., $D_H[k]$ is zero for any k_1, and $D_L[k]$ is zero for any k_2).

2D Fourier-Wavelet Transform, $\Phi\Psi^{-1}$—The fast wavelet transform algorithm can be easily extended to two dimensions using two-dimensional separable convolutions followed by subsamplings (analysis; forward transform), and upsamplings followed by two-dimensional separable convolutions (synthesis; inverse transform). The two-dimensional separable convolution determines the localized k-space data from each wavelet subband n, where n represents one of the four separable two-dimensional filters (e.g., LH consists of low- and high-pass filters, where L represents a low-pass filter between the rows and H represents a high-pass filter between the columns). Figure 2a shows the mapping of wavelet coefficients into k-space data using $\Phi\Psi^{-1}$. High-frequency wavelet subbands (w_{LH}, w_{HL}, w_{HH}) and their localized k-space data (y_{LH}, y_{HL}, y_{HH}) are shown in colors. This mapping of the high-frequency subbands into the k-space regions is determined by spectral weightings (D_{LH}, D_{HL}, D_{HH}), as shown in Fig 2b.

Figure 3 illustrates the 2D Fourier-Wavelet transform $\Phi\Psi^{-1}$, consisting of upsamplings and two-dimensional separable convolutions in frequency domain. If we denote D_n as the spectral weighting between wavelet subbands and k-space regions, and u_n as frequency components of each wavelet coefficients w_n (i.e., $u_n = FT\{w_n\}$), we can describe $\Phi\Psi^{-1}$ as a series of the inverse wavelet transform steps in frequency domain. As shown in Fig 3a, starting from w_n, the localized k-space data y_n can be constructed by a multiplication of D_n and u_{n2},

$$y_n = D_n \cdot u_{n2}, \quad n \in \{LL, LH, HL, HH\}, \quad (9)$$

where u_{n2} is the upsampled version of u_n. The upsampling by two in 2D space is equivalent to replicating four times in frequency domain. Finally, the sum of y_n becomes the k-space data y, as shown in Fig 3b,

$$y = \sum_n y_n. \quad (10)$$

The key here is that if we are able to decompose y into y_n (equivalently, u_n), $\mathcal{F}^{-1}$ can be converted into the individual Fourier transform $\mathcal{F}_s$ between w_n and u_n (i.e., $y = \mathcal{F}^{-1} w$ becomes $u_n = \mathcal{F}_s w_n$). Note that due to the overlap of the spectral weightings D_n, the exact decomposition requires careful sampling. We will show that "quadruplet sampling," in which all four replicas (b_n in Fig. 3a) are sampled, is a sufficient condition for this decomposition.

2D Wavelet Subband Decomposition—As shown previously, u_{n2} is repetitive with respect to u_n, so at a "quadruplet" of locations (b_1, b_2, b_3, and b_4) the values of u_{n2} are identical. An example of a quadruplet set for u_{LH2} is shown in Figure 3a. The k-space data at the quadruplet set can then be formulated in a matrix-vector form by using Eq. 9 and 10:

$$\begin{pmatrix} y[b_1] \\ y[b_2] \\ y[b_3] \\ y[b_4] \end{pmatrix} = \begin{pmatrix} D_{LL}[b_1] & D_{LH}[b_1] & D_{HL}[b_1] & D_{HH}[b_1] \\ D_{LL}[b_2] & D_{LH}[b_2] & D_{HL}[b_2] & D_{HH}[b_2] \\ D_{LL}[b_3] & D_{LH}[b_3] & D_{HL}[b_3] & D_{HH}[b_3] \\ D_{LL}[b_4] & D_{LH}[b_4] & D_{HL}[b_4] & D_{HH}[b_4] \end{pmatrix} \begin{pmatrix} u_{LL}[a] \\ u_{LH}[a] \\ u_{HL}[a] \\ u_{HH}[a] \end{pmatrix} \quad (11)$$

where the matrix, which we refer to as **D**, consists of spectral weightings. Eq. 11 is always invertible because the wavelet filters were designed to satisfy the (bi-)orthogonal conditions of dealiasing and exact reconstruction (31).

When random Fourier undersampling is used, k-space data typically do not always form quadruplet sets (i.e. some of $y(b_1)$, $y(b_2)$, $y(b_3)$, and $y(b_4)$ are missing) and the solution of Eq. 11 may not be always possible to obtain. Although an approximate estimation of u_n may be possible, quadruplet sampling guarantees exact decomposition without much sampling penalty. The wavelet decomposition with quadruplet undersampling enables construction of an independent Fourier relationship between u_n and w_n for each high-frequency wavelet subband. Since the undersampled data y can be decomposed to u_n, with a direct transform to wavelet subband, each u_n can be independently reconstructed using a wavelet sparsity constraint.

Wavelet Tree Structure—The wavelet coefficients can be organized into a tree structure by the nature of concatenated filters (28–30). One easy way to see this is to consider the wavelet transform as a set of local discontinuity detectors: a smooth image region produces small wavelet coefficients while an image region with discontinuities creates a chain of large wavelet coefficients along a branch of the wavelet tree. It follows that the wavelet coefficients are monotonically nonincreasing along the tree branches out from the root. This connected tree property has been successfully exploited in many wavelet-based image compression algorithms.

Figure 4a shows the wavelet tree structure with the tree branches. A wavelet coefficient is non-zero only if the wavelet coefficient in the coarser scale is non-zero (with very few exceptions) (32) and therefore the high-frequency subbands (leaves of the tree) are typically

the most sparse. Secondly, possible non-zero locations of the high-frequency subbands can be limited based on knowledge of the coarser-scale wavelet subbands. Figure 4b illustrates one way to estimate non-zero locations (or support region) of the high-frequency subbands ($j = 2$) using the coarser-scale wavelet subbands ($j = 1$) after applying a wavelet thresholding method, denoted by M_{LH}, M_{HL}, and M_{HH}. After increasing the size twice by duplicating the same binary values, these non-zero location masks can be used as an additional prior for the reconstruction (33).

High-Frequency Subband (HiSub) CS

The wavelet subband decomposition forms a direct Fourier relationship between the decomposed k-space data (u_n) and the high-frequency subband (w_n). We can rewrite Eq. 2 by accommodating this Fourier relationship and non-zero locations:

$$\begin{array}{ll} \text{minimize} & \|w_n\|_1 \\ \text{subject to} & \|\ u_n - \Phi_s w_n\| < \epsilon_n \\ & M_n \cdot w_n = 0, \quad n \in \{LH, HL, HH\} \end{array} \qquad (12)$$

where Φ_s is the smaller random Fourier undersampling, ϵ_n bounds the amount of noise in the subband measurement, and M_n is the estimated non-zeros location mask (1 for non-zeros and 0 for zeros). We named this newly derived minimization problem High-frequency Subband (HiSub) CS, which applies each reconstruction only in a certain k-space region, called the outer k-space region (*LH* or *HL* or *HH*). This local reconstruction method allows us to use a different reconstruction method for the inner k-space region (*LL*). Note that in Eq. 12 the wavelet transform Ψ has been removed, resulting in greatly reduced computational complexity. HiSub CS solves the three independent problems (Eq. 12) where each problem without the wavelet transform is four times smaller than the conventional CS (Eq. 1) minimization. This is advantageous due to smaller memory requirements and the option of parallel computing for independent calculations. Furthermore, the independent reconstruction allows incorporation of different prior knowledge for each wavelet subband such as the non-zero locations based on the wavelet tree structure.

MATERIALS AND METHODS

HiSub CS: Quadruplet Sampling

In the theory section, we have shown that the wavelet subband decomposition is possible if random undersampling forms quadruplet sets. Figure 5a shows a process to generate a quadruplet sampling pattern (k_y-k_z) for HiSub CS. Assuming the full matrix size is $N_y \times N_z$, we first generate four times smaller uniform density random undersampling Φ_s ($N_y/2 \times N_z/2$). Φ_s is duplicated four times (or "tiled") to make the full sized random undersampling. Note that the wavelet subband decomposition is now possible, and Eq. 12 uses Φ_s as the random Fourier undersampling. To accommodate autocalibrating parallel imaging (9, 34) for the low-spatial-frequency content (the inner k-space) estimation, we replace the inner k-space region ($N_y/2 \times N_z/2$) with regular Fourier undersampled data, and finally add a small fully sampled region to allow the kernel calibration.

The HiSub CS undersampling pattern consists of three different k-space regions: a small fully sampled region for the kernel calibration, an inner k-space region for parallel imaging, and an outer k-space region for HiSub CS. The inner k-space region is regularly undersampled (R_{PI}) to estimate low-spatial-frequency content whereas the outer k-space region is randomly undersampled (R_{CS}) to estimate high-spatial-frequency content. An overall reduction factor (R_{net}) is a combination of R_{PI} and R_{CS} including the small fully sampled region. Here, we empirically chose the size of the fully sampled region to be 24 ×

24 ($k_y \times k_z$), R_{PI} to be 2 to 6 depending coil sensitivities, and R_{CS} to be 16. Note that R_{CS} is much higher than R_{PI} due to the wavelet-domain sparsity property in high-frequency subbands.

HiSub CS: Reconstruction

For autocalibrating parallel imaging, we applied autocalibrated reconstruction for Cartesian sampling (ARC) (34). Figure. 5b shows the serial reconstruction of ARC and HiSub CS. We used a regularization factor of 0.01 for the ARC calibration and a kernel size of $3 \times 7 \times 7$ ($k_x \times k_y \times k_z$) for all ARC reconstructions. With ARC, the inner k-space region is recovered well due to the regular undersampling. With HiSub CS, the high-spatial-frequency information is then recovered to restore the fine structure of the image.

After ARC, we can assume the inner k-space region estimated by ARC is fully acquired. Solving Eq. 11 at every point of Ω_s for each high-frequency subband is equivalent to computing:

$$u_n = \Phi_s \tilde{w}_n, \quad n \in \{LH, HL, HH\} \quad (13)$$

where $\tilde{w}_n$ is the high-frequency subband using the image reconstructed using ARC. When the quadruplet sampling is used, this equivalence always stands because frequency components of $\tilde{w}_n$ at the random locations are not perturbed by the analysis process (shown in Fig 1). Once u_n is computed, $\tilde{w}_n$ is only used for the initial guess to solve Eq. 12. Note that this decomposition approach is almost instantaneous and adds only minimal computational cost.

For HiSub CS reconstruction, an approximate message passing (AMP) algorithm (26) was modified to solve Eq. 12 for each of the three subbands. We have added a non-zero location constraint (as shown in Fig 4b) to AMP to improve the reconstruction accuracy (33). The AMP method is a variation of iterative soft-thresholding methods (35–37) and is known to be faster than the conventional L1 minimization algorithms (26). The non-zero location masks M_n were estimated from the coarser scale wavelet coefficients using an adaptive wavelet threshholding method, called VisuShrink (38). The threshholding value was empirically scaled by 1.25 times larger than the value that the wavelet denoising suggests to completely remove small wavelet coefficients in the coarser scale. Any wavelet coefficients above the threshold were considered to be significant, and a binary image (non-zero mask) was set to be one at locations that contained significant wavelet coefficients. The software implementation of the HiSub CS reconstruction is available at http://bmr.stanford.edu/software/. Note that the HiSub CS reconstruction is completely compatible with other CS algorithms (39) that incorporate prior non-zero location information.

For complex-valued images, we used a dual wavelet transform pair: real wavelet coefficients are transformed from the real image and imaginary wavelet coefficients are transformed from the imaginary image. This creates complex-valued wavelet coefficients. HiSub CS minimizes the L1-norm of complex-valued wavelet coefficients in the high-frequency subband, and directly estimates complex-valued wavelet coefficients.

Experimental Methods

All reconstructions were implemented on a Linux PC equipped with a dual six-core 2.66 GHz CPU (Intel Xeon) and 64 GB of memory using Matlab (R2011b; The MathWorks Inc., USA). All MRI experiments were performed on two MR scanners: 1.5T GE Signa Excite and 3.0T GE MR 750 (GE Healthcare, Waukesha WI, USA). We used the normalized root mean squared error (nRMSE) to evaluate the differences between original by the maximum signal of the original:

$$nRMSE = \frac{1}{max(x)} \cdot \sqrt{\frac{1}{N}\sum_{n=1}^{N}(x[n] - \hat{x}[n])^2} \quad (14)$$

where N is the total number of pixels. All reconstructions were performed separately on each coil and the square root of the sum of squares (SOS) was used to combine all the individual coil images. The nRMSE was computed based on the SOS images.

Optimization of Standard CS

The unconstrained L1-minimization of Eq. 1, which we refer to as Standard CS, was solved by using YALL1 (40). YALL1 is a freely available MATLAB software package that provides a collection of fast L1 minimization algorithms based on the dual alternative direction method. The random undersampling densities and the regularization parameters for Standard CS were first examined to find an optimal set that generates the maximum reconstruction accuracy. Two variable density functions were evaluated: an □-valued Gaussian window where the width of the window is inversely related to □ and a power of the distance from the origin. Utilizing the optimal sampling density selected above, we next optimized the regularization parameter. nRMSE was measured 30 times using 30 different regularization values where the values were logarithmically equally spaced between 10^{-4} and 10^{-1}.

HiSub CS: Comparison of ARC, Standard CS, and HiSub CS

An image of a resolution phantom (GE Healthcare) was acquired using a 2D gradient-echo sequence with a matrix size of 512 × 512. A single channel head coil was originally used and the multi-coil images were synthesized by multiplying eight different simulated sensitivity profiles. We assumed the 2D plane to be the *y*-*z* plane to enable two directional random undersampling. We used the Daubechies-6 wavelet transform.

We first compared ARC and Standard CS to show the reconstruction accuracy and the behavior of the residual artifacts as a function of the reduction factor. For Standard CS, we applied the optimal set that was previously selected, and randomly undersampled k-space (repeated 30 times) by a reduction factor of 2 through 9.2. For ARC, we regularly undersampled k-space in both k_y and k_z directions. Each direction was undersampled by a factor of 1 to 3, which created six different reduction factor combinations (minimum of 2 and maximum of 9). The proposed undersampling pattern, described in Figure 5a, was generated 30 times to evaluate two reconstruction methods: ARC and ARC+HiSub CS. The ARC-only method represents good low-spatial-frequency content estimation but poor high-spatial-frequency content estimation, and ARC+HiSub CS is our proposed reconstruction method, which follows the serial reconstruction described in Figure 5b.

HiSub CS: 3D Imaging

High resolution 3D images were acquired with multiple receiver coils for further evaluation. The 3D data were divided into k_y-k_z planes for each *x* location, and each k_y-k_z plane was reconstructed separately. We used the Cohen-Daubechies-Feauveau (CDF) 9/7 wavelet transform, which supports a non-power of two matrix size. We evaluated three reconstruction cases: ARC (regular undersampling), L1-SPIRiT (variable density Poisson-disk sampling) (23), and ARC+HiSub CS (quadruplet sampling). L1-SPIRiT was chosen as an example of a standard CS with PI reconstruction approach using the same overall reduction factor as HiSub CS.

In a grid phantom, we acquired 3D images with a RF-spoiled gradient echo (SPGR) sequence with the following scan parameters: TR/TE = 7.3/5 ms, FOV = 20 cm, matrix = 8 × 512 × 512 ($k_x \times k_y \times k_z$), and BW = 125 kHz. The imaging plane was coronal with a superior-inferior readout direction (the axial plane was the *y-z* plane). A standard 8-channel head coil was used, and the acceleration factor for ARC (R_{PI}) was 2 (1 × 2; $k_y \times k_z$) due to limited coil sensitivity.

For breast imaging, a custom-fitted 16-channel breast array coil was used (41), which enabled parallel imaging in two dimensions (left-right and superior-inferior directions) and R_{PI} was 6 (3 × 2). We acquired high-resolution 3D scans in a total of 7 subjects (four T1-weighted and three T2-weighted scans). For T1-weighted imaging, we used 3D SPGR with fat saturation (matrix size = 360 × 360 × 240) and 3D SPGR (elliptical full k-space; matrix size=252 × 488 × 152). The imaging plane was axial with an anterior-posterior readout direction (the coronal plane was the *y-z* plane). For T2-weighted imaging, we used a 3D FSE sequence in combination with parallel imaging ($k_y \times k_z = 3 \times 2$ and matrix size = 512 × 320 × 152).

RESULTS

HiSub CS: Comparison of ARC, Standard CS, and HiSub CS

Figure 6a shows four reconstruction methods: ARC1, ARC2, Standard CS, and ARC+HiSub CS. ARC2 and ARC+HiSub CS share the same undersampling pattern: the inner region was regularly undersampled by 2 × 2 ($R_{PI} = 4$) and the outer region was randomly undersampled by different reduction factors (R_{CS}) as R_{net} changes. The previous test showed that $R_{PI} = 4$ does not cause any serious residual artifacts. Standard CS has a larger fully sampled region (64 × 64) than HiSub CS (24 × 24) to better phase-correct the complex-valued image.

Figure 6b plots the nRMSE curve (mean ± SD) as a function of the reduction factor for all reconstruction methods. ARC2 has the worst reconstruction performance since it is unable to recover any high-spatial-frequency content. Standard CS has similar performance, but better than ARC2. In all cases, ARC+HiSub CS is superior to all other reconstruction methods and also does not require any data dependent parameter adjustments. This is interesting because the undersampling pattern for Standard CS here is nearly optimal whereas ARC+HiSub CS follows a simple principle of undersampling, which does not require an optimal selection. Note that ARC2 (HiSub CS undersampling) has larger nRMSE than ARC1 (regular undersampling), which confirms parallel imaging works better when regular undersampling is used.

Figure 7 shows the reconstructed images with $R_{net} = 6$ and 10. The high-spatial-frequency content (“comb” shape) and the low-spatial-frequency content (slice thickness bar) are zoomed in to illustrate the separate k-space estimation using the different reconstruction methods. ARC ($R_{PI} = 4$) shows excellent performance recovering both the low- and high-spatial-frequency content. For $R_{net} = 6$, all reconstruction methods show excellent reconstruction accuracy except that Standard CS still includes a few low-resolution residual artifacts. For $R_{net} = 10$, Standard CS shows a resolution loss, while ARC+HiSub CS has good estimation both for the low- and high-spatial-frequency content with the acceptable nRMSE.

HiSub CS: 3D Imaging

Figure 8 shows a reconstruction result for a grid phantom with resolution elements. The reconstructed axial plane (*y-z* plane) image using HiSub CS is similar to the fully-sampled and ARC ($R_{PI} = 2$) images. HiSub CS has a net reduction factor (R_{net}) of 5.8 (R_{CS} is 16 and R_{PI} is 2) and skipping the k-space corners further increases R_{net} to 6.3. The k-space

sampling patterns for all three reconstruction methods are shown at the bottom. The zoomed images at a different location also show that all three reconstructions maintain the fine structure well, indicated by the arrows. The reconstruction time for HiSub CS (excluding the ARC processing) is 2 - 3 seconds per coil.

Figure 9 demonstrates a reconstruction result for high resolution 3D breast imaging. The custom fitted breast coil allows high parallel imaging acceleration with no visible residual artifacts up to $R_{PI} = 6$ (3 × 2). The fully sampled and ARC ($R_{PI} = 6$) images are shown in the axial ($x - y$ plane) and coronal (y-z plane) as a comparison. The ARC+HiSub CS image shows that HiSub CS maintains fine structures (see the arrows) and is close to the fully sampled and ARC acquisitions, even with the extremely high acceleration factor, $R_{net} = 10.7$ ($R_{CS} = 16$ and $R_{PI} = 6$). We applied various undersampling patterns to L1-SPIRiT, including uniform density Poisson-disk sampling and quadruplet sampling, and the variable density Poisson-disk sampling produced the lowest nRMSE. Nonetheless, HiSub CS shows better qualitative reconstruction performance (see the arrows) and has lower nRMSE (0.0152) than L1-SPIRiT (nRMSE = 0.0171). The reconstruction time for HiSub CS is 20 - 30 seconds per coil.

Figure 10 shows an example of T1-weighted images. The fully sampled and ARC images are shown in the coronal (y-z plane) as a comparison. HiSub CS has the similar nRMSE (0.00416) to L1-SPIRiT (nRMSE = 0.00424), but the depiction of fine structures was limited in L1-SPIRiT (see the arrow), while morphology on the HiSub CS image closely resembled the fully sampled and ARC acquisitions. HiSub CS has a net reduction factor (R_{net}) of 12.2 (R_{CS} is 16 and R_{PI} is 6). The reconstruction time for HiSub CS is 40 - 45 seconds per coil.

DISCUSSION

One major advantage of HiSub CS compared with CS is that the reconstruction is localized to parts of k-space, making it more easily separable from (and more compatible with) other local k-space estimation methods such as parallel imaging. Each reconstruction method can be assigned to an appropriate k-space region and an undersampling pattern can be customized for each method. Here, we applied parallel imaging for the low-spatial-frequency region with regular undersampling, and HiSub CS for the high-spatial-frequency region with random quadruplet undersampling.

The initial idea to apply separate reconstructions for each wavelet subband has been described by Candes *et al.* (27). This applies different undersampling factors based on the wavelet subbands to take advantage of the wavelet-domain sparsity. We have expanded the idea by introducing the wavelet subband decomposition using quadruplet undersampling to exactly separate local k-space components. Secondly, we have reformulated the original L1 reconstruction problem into Eq. 12 to exclude the reconstruction of the low-frequency subbands. This allows use of parallel imaging to estimate low-spatial-frequency signal, which avoids any estimation errors (i.e. incoherent artifacts) in low-spatial-frequency content that may result from CS.

Another advantage of HiSub CS is fast reconstruction due to its lower computation cost than CS. HiSub CS removes the wavelet transform in the minimization by reformulating Eq. 1 into Eq. 12 and solves three independent smaller sized problems (four times smaller than original). This lowers the overall computational cost, and in addition, we used the AMP method in conjunction with the non-zero location constraint to further reduce the reconstruction time (26). The reconstruction time using Matlab was around 500 - 800 msec for each 2D plane (512 × 512), which is much faster than conventional L1-minimization

solvers using wavelet transforms. We anticipate further improvements will result from code optimization.

As explained in the theory section, quadruplet sampling is necessary when the exact wavelet subband decomposition is desired. With arbitrary k-space undersampling, approximate wavelet decomposition is still possible due to the nature of the time-frequency localization, and can be done by dividing each subband spectral weighting (i.e. approximate the matrix **D** in Eq. 11 as a diagonal matrix) (27). The reconstruction accuracy using the approximate wavelet decomposition depends on wavelet filters and is slightly lower compared to the reconstruction using the exact wavelet decomposition, but allows more flexible choice of undersampling patterns.

High-frequency subbands typically have smaller amplitudes due to the wavelet tree structure and therefore are more sensitive to noise. When SNR or contrast is not sufficiently high, the reconstruction tends to eliminate more of the wavelet coefficients, resulting in resolution loss. This SNR and contrast limitation is a common issue for both conventional CS and HiSub CS, and HiSub CS is superior to conventional CS methods in various measurement noise levels. High-resolution post contrast imaging, where SNR and contrast are high, is therefore a logical application for HiSub CS.

The serial reconstruction of ARC and HiSub CS can be easily implemented in a modular scheme that generates quick initial feedback (ARC only) and a slower, but better final result (ARC+HiSub CS). This setup could be more attractive in practice since the initial response is quick and has adequate image quality to confirm patient position and successful contrast administration, while a better resolution image is ultimately reconstructed using HiSub CS. This also could be thought of as a resolution enhancement process.

We have chosen a 2D discrete wavelet transform as the sparse transformation but other sparse transformations can be also used for HiSub CS, as long as the transform supports time-frequency localization. A 3D discrete wavelet transform is an easy extension, and can allow better sparsity in the three dimensional domain. The number of high-frequency subbands becomes seven (*LLH*, *LHL*, *LHH*, *HLL*, *HLH*, *HHL*, and *HHH*) instead of three and therefore there are seven different spectral weightings to decompose. HiSub CS would also further reduce the reconstruction time compared to CS, since the 3D wavelet transform is not included in the minimization. Other sparse transformations to consider are dual tree complex wavelets (42), curvelets (43), and contourlets (44), which are known to have better time-frequency localization for images.

Non-decimated wavelet transforms can be another option to consider (45). The non-decimated wavelet transforms can be a better sparse transformation than the discrete wavelet transform due to the noise reduction effects of non-decimated wavelet transforms. However, the quadruplet sampling is not directly applicable for the wavelet subband decomposition since the non-decimated wavelet transforms do not include the downsampling and upsampling steps. In addition, the problem size does not become smaller, and the computational complexity can be either marginally reduced or increased.

HiSub CS can be modified to accommodate additional constraints such as total variation (TV). The iteration process for solving each of the three subbands can be combined to promote the wavelet sparsity at each iteration, and the TV constraint can be enforced after combining the current estimates of the three subbands. However, it may not be possible to take full advantage of exploiting the Wavelet-Fourier transform to lower the computational cost because TV promotes its sparsity based on the image domain (i.e., the inverse wavelet transform should be applied to enforce the TV constraint).

HiSub CS directly estimates complex-valued wavelet coefficients in the high-frequency subband. Because this does not involve any a priori phase estimation processes, the high-spatial-frequency content of phase images can be also recovered. Although we have not acquired any data containing high-spatial-frequency phase variations, we did observe that the phase images using HiSub CS are sharper and finer than the phase images using CS. We believe that any applications that need accurate and high-resolution phase estimation, such as susceptibility weighted imaging and phase contrast imaging, can benefit from this complex-valued minimization.

CONCLUSION

HiSub CS formalizes a direct link between k-space and wavelet domains to enable the use of separate undersampling and reconstruction for inner and outer k-space data. Quadruplet undersampling allows exact separation between two k-space regions based on wavelet subbands. The result is an efficient combination of CS and parallel imaging that can avoid possible CS reconstruction errors in the low-spatial-frequency k-space region, and can improve reconstruction accuracy in high-spatial-frequency k-space regions. This new formulation also reduces the reconstruction time, mostly due to the smaller problem size and replacement of the wavelet transform with a fast Fourier transform in iterations. Applied to high resolution breast imaging, we have demonstrated that HiSub CS can recover fine structures with a net acceleration of 11 to 12.

Acknowledgments

The authors thank Anderson Nnewihe for providing the breast imaging data, Bruce Daniel for his assistance evaluating clinical images, Anja Brau for her assistance for the ARC reconstruction, and Michael Lustig and Marcus Alley for their assistance for the L1 SPIRiT reconstruction.

Grant Sponsors: NIH R01-EB009055; NIH P41-EB015891; GE Healthcare

APPENDIX A: Wavelet Basis Functions

The continuous wavelet transform for a one-dimensional signal $x(t)$ can be described as,

$$W(a,b)=\frac{1}{\sqrt{a}}\int_{-\infty}^{\infty}x(t)\,\psi^{*}\left(\frac{t-b}{a}\right)dt, \quad (15)$$

where $W(a, b)$ is the wavelet coefficient, $\psi^{*}(t)$ is the complex conjugate of the mother wavelet function, and a and b are the scaling and translating parameters. With $a = 2^{j}$ for an integer value of j, the multiresolution representation constructs a series of embedded subspaces V_j, where each V_j has an orthogonal complement, called W_j, in V_{j+1} ($V_j \perp W_{j+1}$; $V_{j+1} = V_j \oplus W_j$). We can now express the space of all measurable, square-integrable functions as the union of infinite vector spaces ($V_j \oplus W_j \oplus W_{j+1} \oplus W_{j+2} \cdots$), and each vector space is spanned by the scaled and translated version of either the scaling function $\varphi(t)$ or wavelet function $\psi(t)$,

$$V_j=Span\left\{\phi_{j,b}(t)\right\}, \quad W_j=Span\left\{\psi_{j,b}(t)\right\}. \quad (16)$$

where we define $\varphi_{j,b}(t) = 2^{j/2}\varphi(2^{j}t - b)$ and $\psi_{j,b}(t) = 2^{j/2}\psi(2^{j}t - \mathrm{b.})$. The multiresolution analysis requires that two basis functions satisfy the following property:

$$\begin{aligned}\phi(t) &= \sum_n h[n]\ \sqrt{2}\phi(2t-n) \\ \psi(t) &= \sum_n g[n]\ \sqrt{2}\phi(2t-n),\end{aligned} \quad (17)$$

where $h[n]$ and $g[n]$ are conjugate mirror filters (low and high pass filters). Note that both functions are designed properly such that we apply a low pass filter $h[n]$ to a basis function of V_1 to construct a basis function of V_0, whereas we apply a high pass filter $g[n]$ to a basis function of V_1 to construct a basis function of W_0.

In the discrete case, a signal $x[n]$, defined in [0, N-1], can be represented using the vector spaces described above,

$$x[n] = \frac{1}{\sqrt{N}} \sum_b c_{j_0}[b]\, \phi_{j_0,b}[n] + \frac{1}{\sqrt{N}} \sum_{j=j_0}^{\infty} \sum_b w_j[b]\, \psi_{j,b}[n] \quad (18)$$

where $c_{j0}[b]$ are the approximation coefficients at an arbitrary starting scale j_0 and $w_j[b]$ are the detailed coefficients. The first sum uses the scaling functions to provide an approximation of $x[n]$ at the scale j_0 and, for each higher scale $j \geq j_0$, the second sum uses the wavelet functions to provide increasing detail to the approximation. The expansion functions form an orthogonal basis, and the wavelet coefficients can be computed by the inner product of $x[n]$ with the basis functions:

$$\begin{aligned}c_{j_0}[b] &= \frac{1}{\sqrt{N}} \sum_n x[n] \cdot \phi_{j_0,b}[n] \\ w_j[b] &= \frac{1}{\sqrt{N}} \sum_n x[n] \cdot \psi_{j,b}[n], \quad j \geq j_0.\end{aligned} \quad (19)$$

This simply shows that any discrete signal $x[n]$ can be decomposed into a set of bandlimited components, called subbands, which can be reassembled to reconstruct the original signal without error.

References

[1]. Scheffler K, Hennig J. Reduced circular field-of-view imaging. Magn. Reson. Med. 1998; 40:474–480. [PubMed: 9727952]

[2]. Peters DC, Korosec FR, Grist TM, Block WF, Holden JE, Vigen KK, Mistretta CA. Undersampled projection reconstruction applied to MR angiography. Magn. Reson. Med. 2000; 43:91–101. [PubMed: 10642735]

[3]. Tsai CM, Nishimura DG. Reduced aliasing artifacts using variable-density k-space sampling trajectories. Magn. Reson. Med. 2000; 43:452–458. [PubMed: 10725889]

[4]. Nayak, KS.; Nishimura, DG. Randomized trajectories for reduced aliasing artifact. Proc., ISMRM, 6th Annual Meeting; Sydney. 1998. p. 670

[5]. Noll DC, Nishimura DG, Macovski A. Homodyne detection in magnetic resonance imaging. IEEE Transactions on Medical Imaging. 1991; 10:154–163. [PubMed: 18222812]

[6]. Haacke EM, Lindskogj ED, Lin W. A fast, iterative, partial-fourier technique capable of local phase recovery. Journal of Magnetic Resonance (1969). 1991; 92:126–145.

[7]. Sodickson DK, Manning WJ. Simultaneous acquisition of spatial harmonics (SMASH): Fast imaging with radiofrequency coil arrays. Magn. Reson. Med. 1997; 38:591–603. [PubMed: 9324327]

[8]. Pruessmann KP, Weiger M, Scheidegger MB, Boesiger P. SENSE: sensitivity encoding for fast MRI. Magn. Reson. Med. 1999; 42:952–962. [PubMed: 10542355]

[9]. Griswold MA, Jakob PM, Heidemann RM, Nittka M, Jellus V, Wang J, Kiefer B, Haase A. Generalized autocalibrating partially parallel acquisitions (GRAPPA). Magn. Reson. Med. 2002; 47:1202–1210. [PubMed: 12111967]

[10]. Candès EJ, Romberg J, Tao T. Robust uncertainty principles: Exact signal reconstruction from highly incomplete frequency information. IEEE Transactions on Information Theory. 2006; 52:489–509.

[11]. Donoho DL. Compressed sensing. IEEE Transactions on Information Theory. 2006; 52:1289–1306.

[12]. Lustig M, Donoho DL, Pauly JM. Sparse MRI: The application of compressed sensing for rapid MR imaging. Magn. Reson. Med. 2007; 58:1182–1195. [PubMed: 17969013]

[13]. Jung H, Ye JC, Kim EY. Improved k–t BLAST and k–t SENSE using FOCUSS. Physics in medicine and biology. 2007; 52:3201–3226. [PubMed: 17505098]

[14]. Jung H, Sung K, Nayak KS, Kim EY, Ye JC. k-t FOCUSS: A general compressed sensing framework for high resolution dynamic MRI. Magn. Reson. Med. 2009; 61:103–116. [PubMed: 19097216]

[15]. Liang, D.; King, KF.; Liu, B.; Ying, L. Accelerating SENSE using distributed compressed sensing. Proc., ISMRM, 17th Annual Meeting; Hawaii. 2009. p. 377

[16]. Beatty, PJ.; King, KF.; Marinelli, L.; Hardy, C.; Lustig, M. Sequential application of parallel imaging and compressed sensing. Proc., ISMRM, 17th Annual Meeting; Hawaii. 2009. p. 2824

[17]. King, KF.; Xu, D.; Brau, AC.; Lai, P.; Beatty, PJ.; Marinelli, L. A new combination of compressed sensing and data driven parallel imaging. Proc., ISMRM, 18th Annual Meeting; Stockholm. 2010. p. 3876

[18]. Liang D, Liu B, Ying L. Accelerating sensitivity encoding using compressed sensing. Conf Proc IEEE Eng Med Biol Soc. 2008:1667–1670. [PubMed: 19162998]

[19]. Liu, B.; Sebert, FM.; Zou, Y.; Ying, L. SparseSENSE: randomly-sampled parallel imaging using compressed sensing. Proc., ISMRM, 16th Annual Meeting; Toronto. 2008. p. 3154

[20]. Ji JX, Zhao C, Lang T. Compressed sensing parallel magnetic resonance imaging. Conf Proc IEEE Eng Med Biol Soc. 2008:1671–1674. [PubMed: 19162999]

[21]. Liang D, Liu B, Wang JJ, Ying L. Accelerating SENSE using compressed sensing. Magn. Reson. Med. 2009; 62:1574–1584. [PubMed: 19785017]

[22]. Otazo R, Kim D, Axel L, Sodickson DK. Combination of compressed sensing and parallel imaging for highly accelerated first-pass cardiac perfusion MRI. Magn. Reson. Med. 2010; 64:767–776. [PubMed: 20535813]

[23]. Lustig M, Pauly JM. SPIRiT: Iterative self-consistent parallel imaging reconstruction from arbitrary k-space. Magn. Reson. Med. 2010; 64:457–471. [PubMed: 20665790]

[24]. Wu B, Millane RP, Watts R, Bones PJ. Prior estimate-based compressed sensing in parallel MRI. Magn. Reson. Med. 2011; 65:83–95. [PubMed: 21031492]

[25]. Donoho DL, Tanner J. Observed universality of phase transitions in high-dimensional geometry, with implications for modern data analysis and signal processing. Philosophical Transactions of the Royal Society A: Mathematical, Physical and Engineering Sciences. 2009; 367:4273–4293.

[26]. Donoho DL, Maleki A, Montanari A. Message-passing algorithms for compressed sensing. Proceedings of the National Academy of Sciences. 2009; 106:18914–18919.

[27]. Candès EJ, Romberg J. Sparsity and incoherence in compressive sampling. Inverse Problems. 2007; 23:969–985.

[28]. Cohen A, Dahmen W, Daubechies I, DeVore R. Tree approximation and optimal encoding. Applied and Computational Harmonic Analysis. 2001; 11:192–226.

[29]. Romberg JK, Choi H, Baraniuk RG. Bayesian tree-structured image modeling using wavelet-domain hidden Markov models. IEEE Transactions on Image Processing. 2002; 10:1056–1068. [PubMed: 18249679]

[30]. Portilla J, Strela V, Wainwright MJ, Simoncelli EP. Image denoising using scale mixtures of Gaussians in the wavelet domain. Image Processing, IEEE Transactions on. 2003; 12:1338–1351.

[31]. Vetterli M. Filter banks allowing perfect reconstruction. Signal Processing. 1986; 10:219–244.

[32]. Baraniuk RG, DeVore RA, Kyriazis G, Yu XM. Near best tree approximation. Advances in Computational Mathematics. 2002; 16:357–373.

[33]. Sung, K.; Daniel, BL.; Hargreaves, BA. Location constrained approximate message passing (LCAMP) algorithm for compressed sensing. Proc., ISMRM, 19th Annual Meeting; Montreal. 2011. p. 72

[34]. Brau, AC.; Beatty, PJ.; Skare, S.; Bammer, R. Efficient computation of auto calibrating parallel imaging reconstruction. Proc., ISMRM, 14th Annual Meeting; Seattle. 2006. p. 2462

[35]. Fornasier M, Rauhut H. Iterative thresholding algorithms. Applied and Computational Harmonic Analysis. 2008; 25:187–208.

[36]. Blumensath T, Davies ME. Iterative hard thresholding for compressed sensing. Applied and Computational Harmonic Analysis. 2009; 27:265–274.

[37]. Needell D, Tropp JA. CoSaMP: Iterative signal recovery from incomplete and inaccurate samples. Applied and Computational Harmonic Analysis. 2009; 26:301–321.

[38]. Donoho DL, Johnstone JM. Ideal spatial adaptation by wavelet shrinkage. Biometrika. 1994; 81:425–455.

[39]. Miosso C, von Borries R, Argaez M, Velazquez L, Quintero C, Potes C. Compressive sensing reconstruction with prior information by iteratively reweighted least-squares. IEEE Transactions on Signal Processing. 2009; 57:2424–2431.

[40]. Yang, J.; Zhang, Y. Alternating direction algorithms for l1-problems in compressive sensing. Rice University; 2009. Technical Report

[41]. Nnewihe A, Grafendorfer T, Daniel B, Calderon P, Alley M, Robb F, Hargreaves B. Custom-fitted 16-channel bilateral breast coil for bidirectional parallel imaging. Magn. Reson. Med. 2011

[42]. Selesnick IW, Baraniuk RG, Kingsbury NC. The dual-tree complex wavelet transform. Signal Processing Magazine, IEEE. 2005; 22:123–151.

[43]. Starck JL, Candès EJ, Donoho DL. The curvelet transform for image denoising. IEEE Transactions on Image Processing. 2002; 11:670–684. [PubMed: 18244665]

[44]. Do M, Vetterli M. The contourlet transform: an efficient directional multiresolution image representation. IEEE Transactions on Image Processing. 2005; 14:2091–2106. [PubMed: 16370462]

[45]. Fowler J. The redundant discrete wavelet transform and additive noise. IEEE Signal Processing Letters. 2005; 12:629–632.

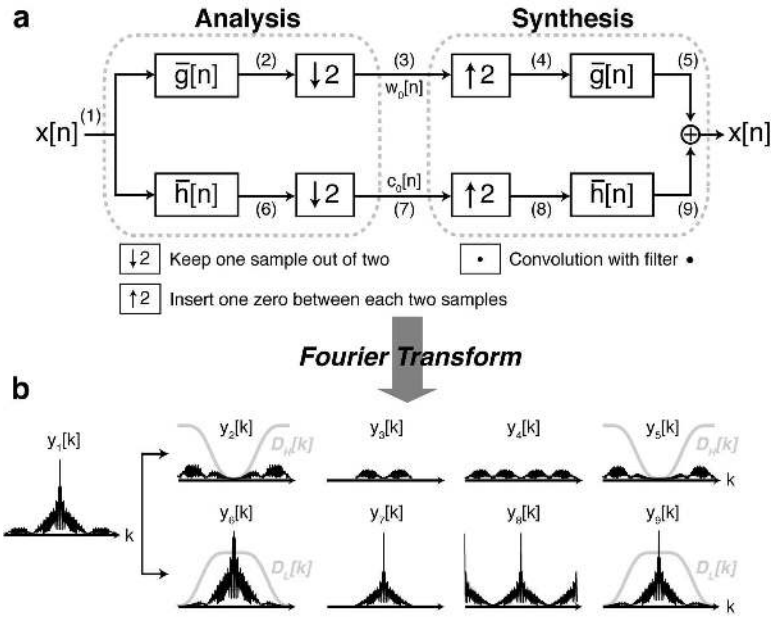

Figure 1.

1D discrete wavelet transform using an orthogonal basis: (a) the schematic diagram to realize the fast wavelet transform with a single scale, and (b) its behavior in frequency domain.

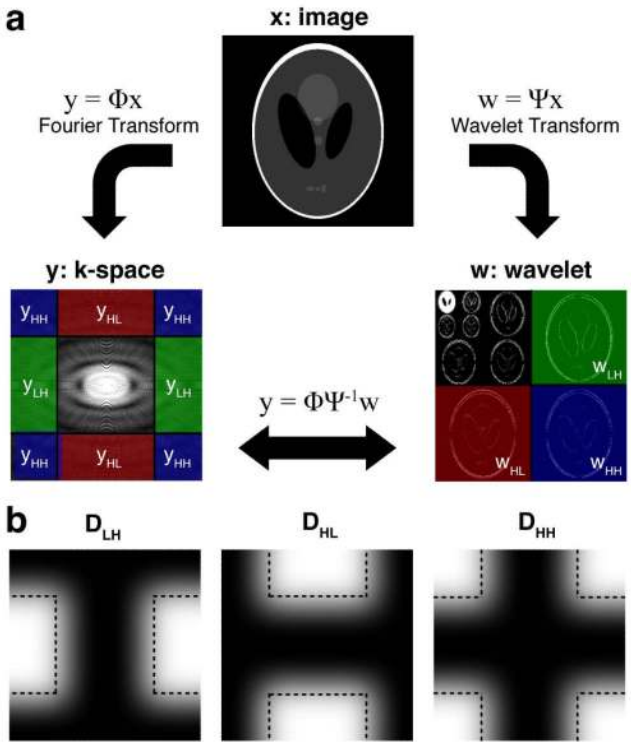

Figure 2.
Illustration of the domains used in CS MRI and the property of wavelet transforms. (a) The relationship among three domains (x: image, y: k-space, and w: wavelet). High-frequency subbands and the corresponding k-space data are colored (*LH*: green, *HL*: red, and *HH*: blue). (b) High-frequency subband spectral weightings. The Daubechies-6 wavelet has been used here and an ideal set of the zero-transition-band filters is indicated by the dotted lines.

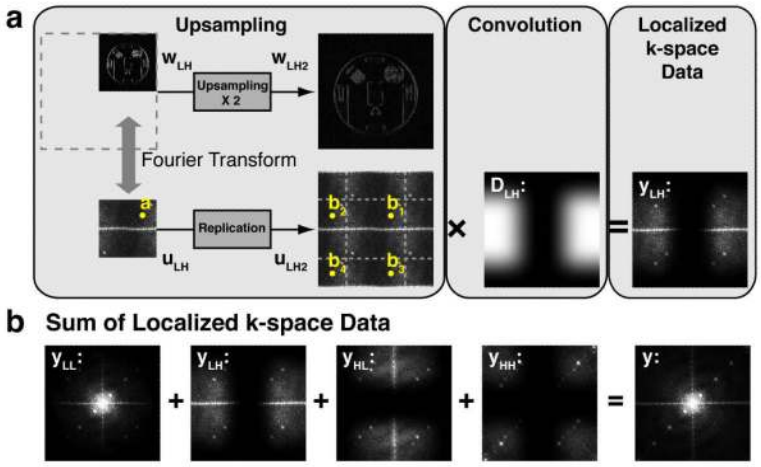

Figure 3.

Illustration of the 2D Fourier-Wavelet transform, $\mathcal{F}\mathcal{W}^{-1}$, consisting of (a) 2D upsampling and convolution, and (b) the sum of the localized k-space data. The upsampling in 2D space is the same as the replication in frequency domain, and the 2D convolution is the same as the multiplication of the spectral weighting D_n in frequency domain. The sum of all the localized k-space data regions (y_n) becomes a full k-space data set (y).

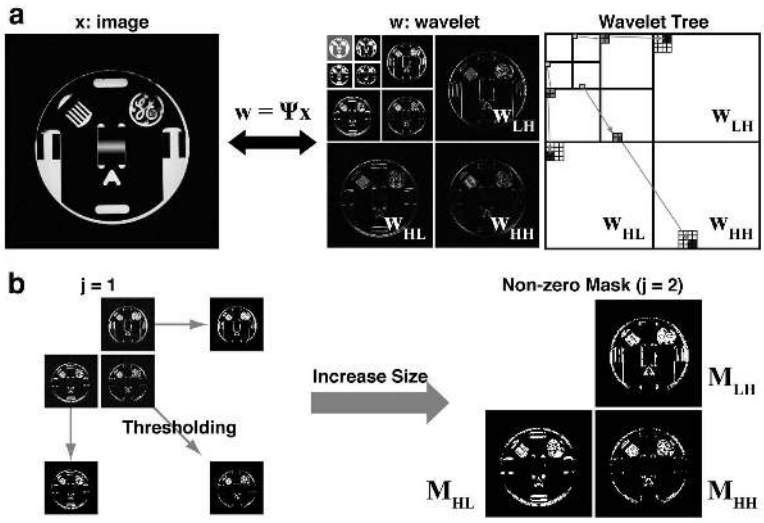

Figure 4.
Illustration of (a) the wavelet tree structure and (b) the non-zero location estimation. Wavelet coefficients naturally form a tree structure flowing from the coarsest scale to the finest scale, described by the arrows, and are typically non-increasing along the branches of the tree. This results in two main observations: the high-frequency subbands are the most sparse, and possible non-zero locations of the high-frequency subbands are limited by the coarser scale wavelet subbands.

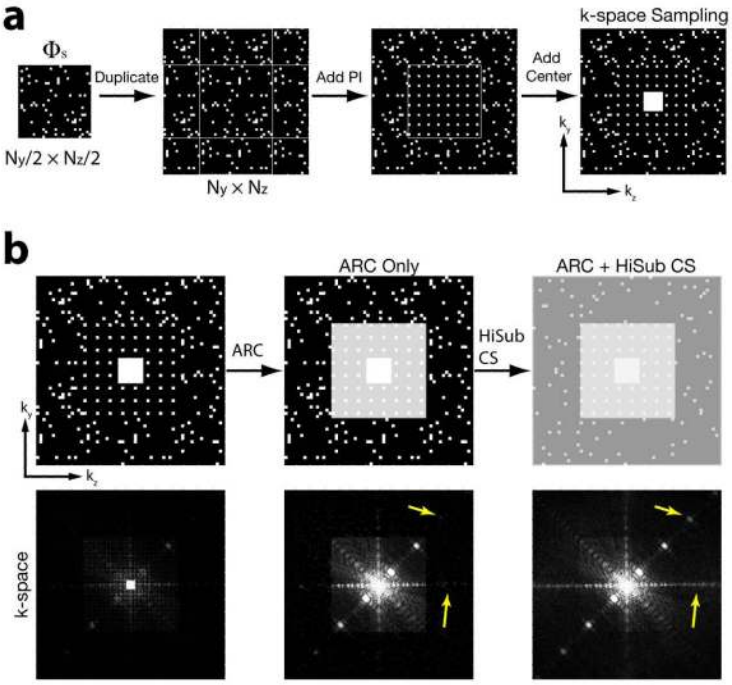

Figure 5.

HiSub CS: quadruplet sampling and reconstruction. (a) The generation of k-space undersampling consists of the duplication of Φ_s, the addition of regular undersampling, and the addition of a fully sampled region. The proposed undersampling pattern is customized to accommodate the separate reconstruction methods, CS and parallel imaging. (b) The serial reconstruction of ARC and HiSub CS shows how each reconstruction method recovers two different k-space regions (low- and high-spatial-frequency contents).

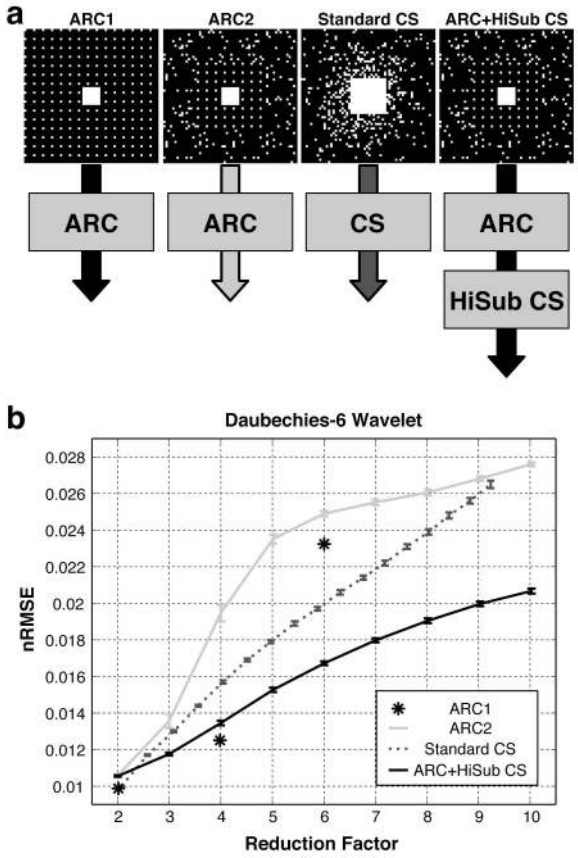

Figure 6.

Comparison of ARC, Standard CS and ARC+HiSub CS: (a) illustration of each method with associated k-space undersampling patterns and (b) nRMSE (mean ± SD) plots with different reduction factors. For all reduction factors, ARC+HiSub CS shows the best performance based on this metric.

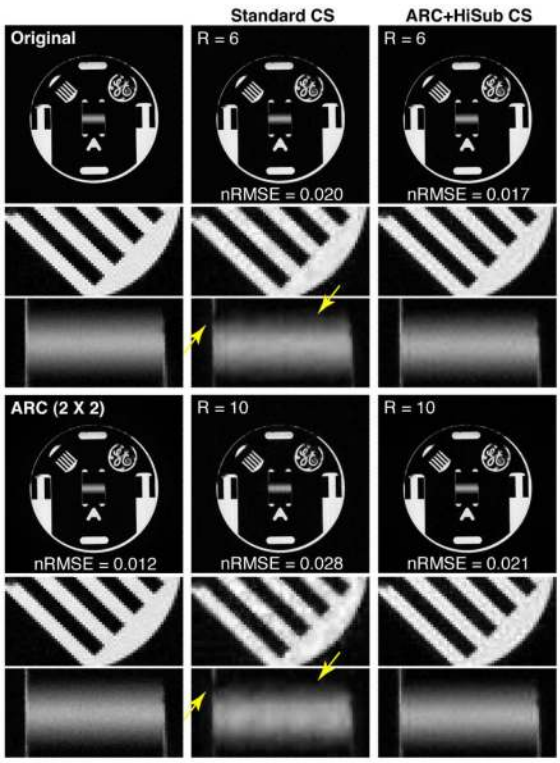

Figure 7.
Reconstruction examples of the two methods (Standard CS and ARC+HiSub CS). The original image and ARC (2 × 2) are shown on the left as references. Different regions of reconstructed images are zoomed in to better depict high-frequency (comb shape) and low-frequency (slice thickness bar) contents. For R = 6 and R = 10, Standard CS contains residual artifacts, indicated by the arrows, while ARC+HiSub CS shows excellent reconstruction.

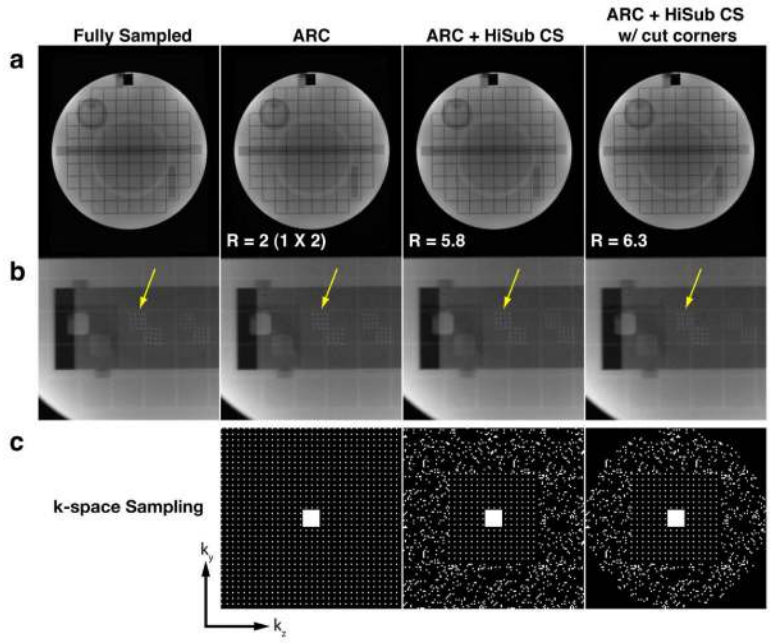

Figure 8.

High-resolution 3D grid phantom images using the three reconstruction methods: ARC, ARC+HiSub CS, ARC+HiSub CS with cutting the k-space corners. (a) Reconstructed images, (b) zoomed-in versions of reconstructed images in a different slice location and (c) associated k-space undersampling schemes. Note that an example of high-resolution features, indicated by the arrows, is well maintained.

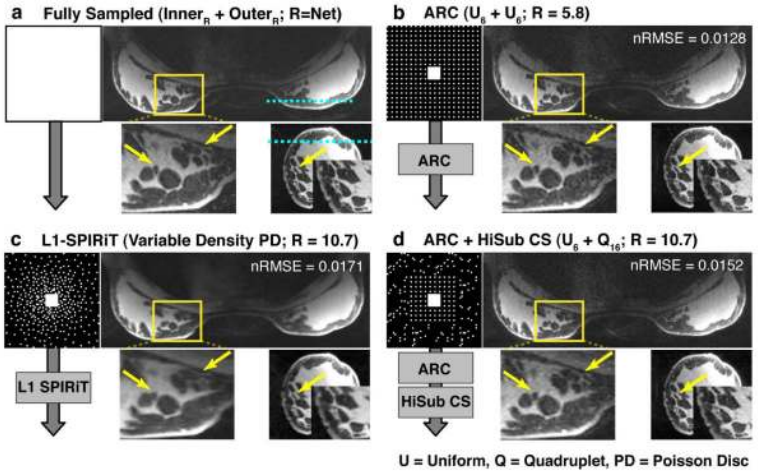

Figure 9.

High-resolution 3D breast imaging with fat saturation using the different reconstruction methods: (a) fully sampled, (b) ARC (R = 5.8), (c) L1-SPIRiT (R = 10.7), and (d) ARC +HiSub CS (R = 10.7). The k-space undersampling patterns are placed on the left to describe different $k_y - k_z$ sampling schemes for different reconstruction methods. Note that L1-SPIRiT and HiSub CS have the different sharpness of the breast images (see the arrows).

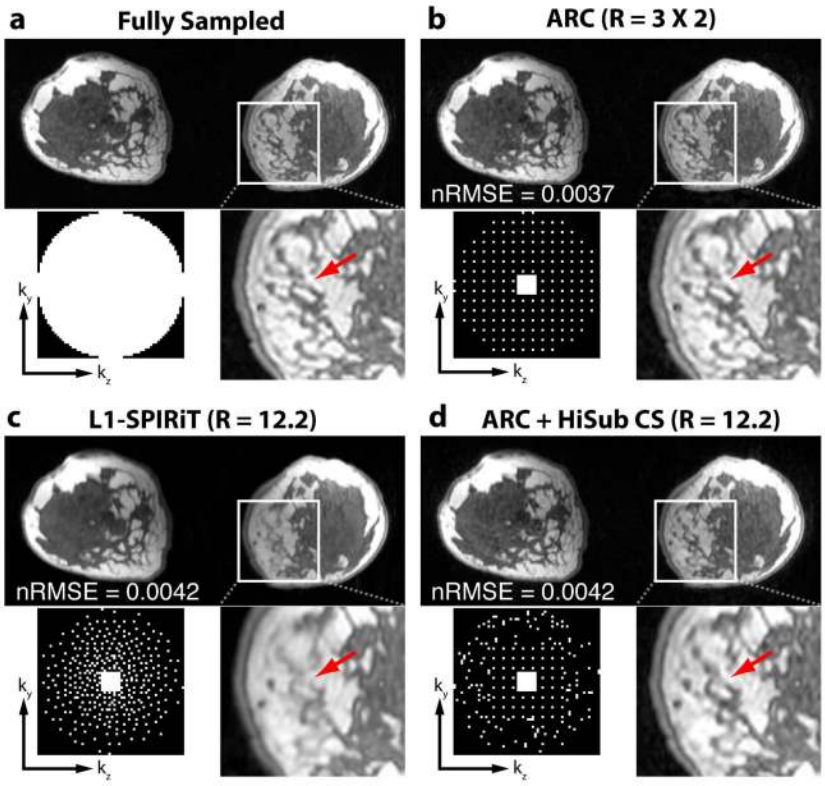

Figure 10.
High-resolution 3D T1-weighted breast imaging without fat saturation using: (a) fully sampled, (b) ARC (R = 5.8), (c) L1-SPIRiT (R = 12.2), and (d) ARC+HiSub CS (R = 12.2). Images are shown in the coronal plane, and fine structures are magnified to show the differences (see the arrows).